

The Computation of MR Image Distortions Caused by Tissue Susceptibility Using the Boundary Element Method

J. C. de Munck,* R. Bhagwandien, S. H. Muller, F. C. Verster, and M. B. van Herk

Abstract— Static field inhomogeneity in magnetic resonance (MR) imaging produces geometrical distortions which restrict the clinical applicability of MR images, e.g., for planning of precision radiotherapy. The purpose of this paper is to describe a method to compute distortions which are caused by the difference in magnetic susceptibility between the scanned object and the surrounding air. Such a method is useful for understanding how the distortions depend on the object geometry, and for correcting for geometrical distortions, and thereby improving MR/CT registration algorithms. The geometric distortions in MR can be directly computed from the magnetic field inhomogeneity and the applied gradients. The boundary value problem of computing the magnetic field inhomogeneity caused by susceptibility differences is analyzed. It is shown that the boundary element method (BEM) has several advantages over previously applied methods to compute the magnetic field. Starting from the BEM and the assumption that the susceptibilities are very small (typically $O(10^{-5})$ or less), a formula is derived to compute the magnetic field directly, without the need to solve a large system of equations. The method is computationally very efficient when the magnetic field is needed at a limited number of points, e.g., to compute geometrical distortions of a set of markers or a single surface. In addition to its computational advantage the method proves to be efficient to correct for the lack of data outside the scan which normally causes large artifacts in the computed magnetic field. These artifacts can be reduced by assuming that at the scan boundary the object extends to infinity in the form of a generalized cylinder. With the adaptation of the BEM this assumption is equivalent to simply omitting the scan boundary from the computations. To our knowledge, no such simple correction method exists for other computation methods. The accuracy of the algorithm was tested by comparing the BEM solution with the analytical solution for a sphere. When the applied homogeneous field is 1.5 T the agreement between both methods was within $0.11 \cdot 10^{-6}$ T. As an example, the method was applied to compute the displacement vector field of the surface of a human head, derived from an MR imaging data set. This example demonstrates that the distortions can be as large as 3 mm for points just outside the head when

a gradient strength of 3 mT/m is used. It was also observed that distortion within the head can be described accurately as a linear scaling in the axial direction.

I. INTRODUCTION

An important cause of geometrical distortions in magnetic resonance (MR) imaging is the presence of inhomogeneities in the applied magnetic field, e.g., [1], [16], [18], [19], [29]. Depending on the specific configuration of the MR scanner, the amplitude of these distortions can be as large as several pixels [1], [2], [16], [19], [21]. Distortions of this size are a limiting factor for high-precision applications such as stereotactic neurosurgery [22], [23] and radiotherapy treatment planning [24]–[26]. With the latter technique, MR is used to localize the tumor and to determine its extension, whereas computed tomography (CT) is used to plan the dose distribution.

Field inhomogeneities caused by susceptibility differences between the scanned object and surrounding air cannot be compensated by calibration of the scanner. However, techniques exist to restore MR images based on the knowledge of the magnetic field inhomogeneities [2], [3], [29]. For this reason, it is important to have an efficient method for computing magnetic field inhomogeneities caused by the scanned object. Moreover, such a method is useful in investigating whether image distortions are clinically important for a given object and for a given MR scanning configuration.

A previous method to compute the magnetic field inhomogeneities is based on the finite difference method [4], [5]. In this method the differential equation for the magnetic field is approximated by the differences between potentials on a rectilinear or curvilinear three-dimensional (3-D) grid. These differences yield a set of linear equations that can be solved iteratively. Since the number of equations equals the number of grid points the computation time can be quite large. Other methods, like the finite element method [6] and the finite volume method [7] are also based on a 3-D grid and therefore their computational cost will be comparable.

The main purpose of this paper is to reduce the computational cost involved with these calculations. When it is assumed that the object consists of compartments of isotropic and constant susceptibility the boundary element method (BEM) can be used to compute the magnetic field inhomogeneities, as will be shown in Section II. With this

Manuscript received December 6, 1995; revised July 1, 1996. This work was supported by the Dutch Cancer Foundation under Grant NKI 94777. The Associate Editor responsible for coordinating the review of this paper and recommending its publication was M. Viergever. Asterisk indicates corresponding author.

*J. C. DeMunck is with The Netherlands Cancer Institute (Antoni van Leeuwenhoek Huis), Plesmanlaan 121, 1066 CX Amsterdam, The Netherlands (e-mail jdemunck@nki.nl).

R. Baghawandien is with the Academic Hospital Utrecht, Department of Radiation Therapy, 3500 GA Utrecht, The Netherlands.

S. H. Muller, F. C. Verster, and M. B. van Herk are with The Netherlands Cancer Institute (Antoni van Leeuwenhoek Huis), Plesmanlaan 121, 1066 CX Amsterdam, The Netherlands.

Publisher Item Identifier S 0278-0062(96)07298-9.

method the total magnetic field is split into a homogeneous field, which is known, and a perturbation field, for which a boundary integral equation is valid. In this equation, the unknown perturbation field appears only on a set of two-dimensional (2-D) surfaces and therefore the discretization can be derived from a set of 2-D grids. The resulting linear system of equations is much smaller than in the 3-D methods. Moreover, it appears that when the susceptibility differences are small (such as in human tissue) an approximation of the BEM can be used, in which the magnetic field is computed directly without the need to solve a system of equations at all.

II. METHODS

A. Formulation of the Problem

When an object is placed in a homogeneous magnetic induction field \mathbf{B}_0 , a distortion of this field will occur, depending on the susceptibility distribution, $\chi(\mathbf{x})$, of the object. The field distortion or perturbation field is represented in this paper with the symbol \mathbf{B}_P . The total magnetic induction, $\mathbf{B} = \mathbf{B}_0 + \mathbf{B}_P$, satisfies

$$\nabla \cdot \mathbf{B} = \nabla \cdot (\mathbf{B}_0 + \mathbf{B}_P) = 0. \quad (1)$$

The magnetic induction is related to the magnetic field, \mathbf{H} , by

$$\mathbf{B} = \mu_0(1 + \chi)\mathbf{H} \quad (2)$$

where μ_0 is the magnetic permeability of vacuum. Due to time-invariance and the absence of stationary currents the curl of \mathbf{H} vanishes and \mathbf{H} can be expressed as the gradient of a magnetic scalar potential U

$$\mathbf{H} = \nabla U \quad (3)$$

and hence

$$\mathbf{B} = \mu_0(1 + \chi)\nabla U. \quad (4)$$

The magnetic potential is split into a part corresponding to the driving potential U_0 which is known and a perturbation potential U_P which is to be computed. It follows from (1) and (4) that U_P satisfies

$$\nabla \cdot ((1 + \chi)\nabla U_P) = -\nabla \cdot ((1 + \chi)\nabla U_0). \quad (5)$$

Here, it should be noted that χ depends on the position \mathbf{x} . When it is assumed that the object consists of compartments in which the susceptibility is constant, the potential U satisfies the Laplace equation, $\Delta U = \Delta U_P + \Delta U_0 = 0$. But since $\Delta U_0 = 0$, by definition, it follows that the perturbed potential U_P satisfies the Laplace equation, $\Delta U_0 = 0$, for \mathbf{x} inside these regions. From Maxwell's equations it follows that at the interfaces between compartments of different susceptibility the tangential component of the total magnetic induction and the normal component of the total magnetic field are continuous.

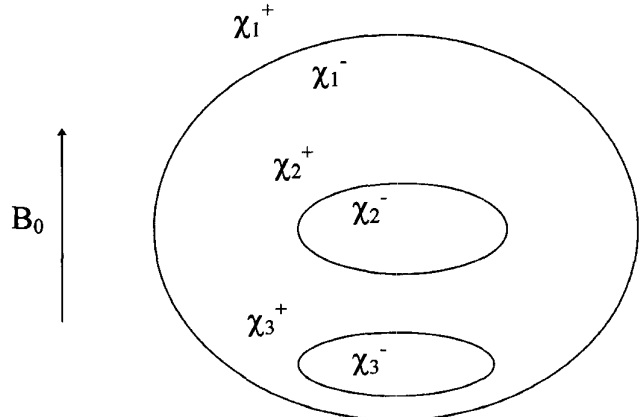


Fig. 1. A sketch of the geometry and the meaning of the symbols in the boundary element method. The object is divided into compartments in which the susceptibility is constant and isotropic. The surfaces separating two compartments are represented by S_1, S_2, S_3 , etc. The susceptibilities at each side of a boundary are given by $\chi_1^+, \chi_1^-, \chi_2^+, \chi_2^-, \chi_3^+, \chi_3^-$, etc. Note that different symbols may denote the susceptibility of the same compartment. For example, in Fig. 1 we have $\chi_1^- = \chi_2^- = \chi_3^+$.

In terms of U this implies that, respectively

$$U_{\text{inside}} = U_{\text{outside}} \quad (6)$$

and

$$(1 + \chi_{\text{inside}})(\nabla U \cdot d\mathbf{S})_{\text{inside}} = (1 + \chi_{\text{outside}})(\nabla U \cdot d\mathbf{S})_{\text{outside}}. \quad (7)$$

Here $d\mathbf{S}$ is a surface element of the interface separating two compartments; see [27].

B. The Boundary Element Method

The boundary value problem defined by $\Delta U_P = 0$ with boundary conditions (6) and (7) is almost equivalent to the mathematical problem of computing the electric potential distribution in a volume conductor with a piecewise constant conductivity distribution (see e.g., [8]). This problem arises in theoretical studies of the generators of the electrocardiogram (ECG) and electroencephalogram (EEG) [9], [10]. In [8] a derivation of an equivalent boundary integral equation is presented. With some adaptations, it is found that for the present magnetic field problem the following boundary integral equation is valid

$$4\pi \left(1 + \frac{\chi_j^+ + \chi_j^-}{2} \right) U_P(\mathbf{x}) = \sum_{k=1}^K (\chi_k^+ - \chi_k^-) \iint_{S_k} \left(\frac{1}{r} \nabla' U_0 + U_P(\mathbf{x}') \nabla' \frac{1}{r} \right) \cdot d\mathbf{S}' \quad \text{for } \mathbf{x} \in S_j \text{ and } j = 1, \dots, K. \quad (8)$$

Here, S_j are the surfaces enclosing the compartments and χ_j^+ and χ_j^- are the susceptibilities just outside and inside the j -th surface (see Fig. 1). The summation is over all K surfaces. Finally, $r \equiv |\mathbf{x} - \mathbf{x}'|$ and ∇' is the gradient with respect to

the integration variable \mathbf{x}' (which in this case takes the form of a surface element $d\mathbf{S}'$).

Equation (8) is an integral equation in the function $U_P(\mathbf{x})$ because this variable appears on both the right- and left-hand side. Once this equation is solved, the result can be substituted into

$$\begin{aligned} 4\pi(1+\chi)U_P(\mathbf{x}) &= \sum_{k=1}^K (\chi_k^+ - \chi_k^-) \\ &\times \iint_{S_k} \left(\frac{1}{r} \nabla' U_0 + U_P(\mathbf{x}') \nabla' \frac{1}{r} \right) \cdot d\mathbf{S}' \\ &\quad \text{for } \mathbf{x} \notin S_j \end{aligned} \quad (9)$$

to obtain the perturbation potential at any other position \mathbf{x} . Here, χ at the left-hand side is the susceptibility at \mathbf{x} . Note that in the right-hand side of (9) U_P is evaluated at the interfaces, whereas, on the left-hand side it is evaluated for \mathbf{x} inside a compartment.

The boundary integral equation (8) is discretized by describing the surfaces S_j with a finite number of vertices. These vertices are connected by edges in such a way that each surface is covered by a set of nonoverlapping triangles of which the union is an approximation of the surface. This triangulation is used to derive a set of base functions $h_n(\mathbf{x})$ in which the unknown $U_P(\mathbf{x})$ is expanded with coefficients u_n

$$U_P(\mathbf{x}) \approx \sum_{n=1}^N u_n h_n(\mathbf{x}) \quad (10)$$

where N is the number of vertices. It is convenient to choose the base functions $h_n(\mathbf{x})$ in such a way that they are equal to one on vertex \mathbf{x}_n and vary linearly over each adjoining triangle to zero [11] at the opposing edge. On all other triangles $h_n(\mathbf{x})$ is zero. The following base functions satisfy these conditions:

$$h_n(\mathbf{x}) = \begin{cases} \frac{\det(\mathbf{x}_l, \mathbf{x}_m, \mathbf{x})}{\det(\mathbf{x}_l, \mathbf{x}_m, \mathbf{x}_n)} & \text{for } \mathbf{x} \in \Delta_{lmn} \\ 0 & \text{otherwise} \end{cases} \quad (11)$$

where \mathbf{x}_l , \mathbf{x}_m , and \mathbf{x}_n are vertices of the grid which form triangle Δ_{lmn} and $\det(\mathbf{x}_l, \mathbf{x}_m, \mathbf{x}_n)$ is the determinant of the 3×3 matrix with columns \mathbf{x}_l , \mathbf{x}_m , and \mathbf{x}_n .

When (10) is substituted into the boundary integral equation (8), and \mathbf{x} is varied over the vertices $\{\mathbf{x}_n\}$, so that $U_S(\mathbf{x}_n) = u_n$, a linear system of equations is derived in which the u_n coefficients appear as unknowns and

$$v_n = \sum_k (\chi_k^+ - \chi_k^-) \iint_{S_k} \frac{\nabla' U_0(\mathbf{x}')}{|\mathbf{x}_n - \mathbf{x}'|} \cdot d\mathbf{S}' \quad (12)$$

appears as the (known) right-hand side. If we write

$$\sum_{m=1}^N a_{nm} u_m = v_n \quad (13)$$

the matrix elements a_{nm} can be expressed as

$$\begin{aligned} a_{nm} &= -(\chi_n^+ - \chi_n^-) \times \\ &\quad \iint_{S_k} h_m(\mathbf{x}') \nabla' \frac{1}{|\mathbf{x}_n - \mathbf{x}'|} \cdot d\mathbf{S}' \\ &\quad + 4\pi \left(1 + \frac{\chi_n^+ + \chi_n^-}{2} \right) \delta_{nm} \end{aligned} \quad (14)$$

where δ_{nm} is the Kronecker delta. The susceptibilities in the first term of (14) refer to the positive and negative side of the surface through \mathbf{x}_m , whereas, the susceptibilities in the second term are taken at the positive and negative side of the surface through \mathbf{x}_n . Note that since the base functions $h_m(\mathbf{x})$ are nonzero only nearby the vertex \mathbf{x}_m , the surface integral in (14) extends only over the triangles adjacent to the point \mathbf{x}_m .

C. An Approximation for $\chi \rightarrow 0$

The normal procedure to solve the differential equation using the BEM is to compute the matrix elements, solve the system of equations and substitute the solution into a discretized version of (9). However, with clinical MR imaging the parameters χ_k are extremely small, typically of the order of 10^{-5} or less. This fact can be used to find a simple approximate solution. The size of the integrals in (14) can be estimated as follows

$$\begin{aligned} &\left| \iint_{S_k} h_m(\mathbf{x}') \nabla' \frac{1}{|\mathbf{x}_n - \mathbf{x}'|} \cdot d\mathbf{S}' \right| \\ &\leq \iint_{S_k} |h_m(\mathbf{x}')| \left| \nabla' \frac{1}{|\mathbf{x}_n - \mathbf{x}'|} \cdot d\mathbf{S}' \right| \\ &< \sum_i |\Omega_{m,i,i+1}(\mathbf{x}_n)| < 2I\pi. \end{aligned} \quad (15)$$

Here it is used that $|h_m(x)| \leq 1$; $\Omega_{m,i,i+1}(\mathbf{x}_n)$ is the solid angle of triangle $\Delta_{m,i,i+1}$ subtended at vertex \mathbf{x}_n ; I is the number of triangles adjacent to vertex \mathbf{x}_n , which is typically about six.

From (15) it follows that the ratio of the magnitudes of the first and second term of (14) is of the order of $\chi_k^+ - \chi_k^-$. Hence we find that for $\chi_k \rightarrow 0$ all off-diagonal elements vanish and that $a_{nm} \rightarrow 4\pi\delta_{nm}$. The solution of (13) tends to $u_m \rightarrow v_m/(4\pi)$, which is proportional to the susceptibility differences, as follows from (12). The conclusion is that in (9) the second surface integral is negligible with respect to the first and so the perturbation magnetic potential may be directly computed from

$$U_P(x) \approx \frac{1}{4\pi} \sum_k (\chi_k^+ - \chi_k^-) \iint_{S_k} \frac{1}{|\mathbf{x}' - \mathbf{x}|} \nabla' U_0 \cdot d\mathbf{S}'. \quad (16)$$

To compute the perturbation field one can use that $\mathbf{B}_P \equiv \mu_0(1+\chi)\nabla(U_0 + U_P) - \mathbf{B}_0 \approx \chi\mathbf{B}_0 + \mu_0\nabla U_P$. So one finds

$$\mathbf{B}_P(\mathbf{x}) \approx \chi\mathbf{B}_0 + \frac{1}{4\pi} \sum_{k=1}^K (\chi_k^+ - \chi_k^-) \nabla \iint_{S_k} \frac{1}{|\mathbf{x}' - \mathbf{x}|} \mathbf{B}_0 \cdot d\mathbf{S}'. \quad (17)$$

To compute the surface integrals in (17) in practice, they are first approximated as a sum of integrals over the triangles described before. It appears that these triangle integrals can be expressed in closed analytical form, similar to the integrals Ω and $\tilde{\Omega}$ presented in [11], as follows. First the derivative ∇ with respect to \mathbf{x} can be replaced by a derivative with respect to \mathbf{x}' if simultaneously a minus sign is added. Next, it can be used that \mathbf{B}_0 is constant and that we have the identity

$(\mathbf{n} \cdot \mathbf{n})\mathbf{g} \equiv \mathbf{n} \times (\mathbf{g} \times \mathbf{n}) + \mathbf{n}(\mathbf{g} \cdot \mathbf{n})$, for any two vectors \mathbf{n} and \mathbf{g} . In this way it is found for $\mathbf{x} \notin S_k$

$$\begin{aligned}\mathbf{B}_P(\mathbf{x}) &= \chi(\mathbf{x})\mathbf{B}_0 - \frac{1}{4\pi} \sum_j (\chi_{kj}^+ - \chi_{kj}^-) \mathbf{B}_0 \cdot \mathbf{n}_j \\ &\quad \times (\mathbf{n}_j \times \vec{\Omega}_j(\mathbf{x}) + \mathbf{n}_j \Omega_j(\mathbf{x})).\end{aligned}\quad (18)$$

Here the summation is over all triangles and k_j is the surface index corresponding to triangle j . Furthermore, \mathbf{n}_j is the normal of the j th triangle

$$\mathbf{n} = \frac{\mathbf{x}_1 \times \mathbf{x}_2 + \mathbf{x}_2 \times \mathbf{x}_3 + \mathbf{x}_3 \times \mathbf{x}_1}{|\mathbf{x}_1 \times \mathbf{x}_2 + \mathbf{x}_2 \times \mathbf{x}_3 + \mathbf{x}_3 \times \mathbf{x}_1|} \quad (19)$$

and with $\mathbf{y}_i \equiv \mathbf{x}_i - \mathbf{x}$

$$\begin{aligned}\Omega_j(\mathbf{x}) &= \iint_{\Delta_j} \nabla' \frac{1}{|\mathbf{x}' - \mathbf{x}|} \cdot d\mathbf{S}' \\ &= 2 \arctan \frac{\det(\mathbf{y}_1, \mathbf{y}_2, \mathbf{y}_3)}{|\mathbf{y}_1||\mathbf{y}_2||\mathbf{y}_3| + |\mathbf{y}_1|\mathbf{y}_2 \cdot \mathbf{y}_3 + |\mathbf{y}_2|\mathbf{y}_3 \cdot \mathbf{y}_1 + |\mathbf{y}_3|\mathbf{y}_1 \cdot \mathbf{y}_2}\end{aligned}\quad (20)$$

is the solid angle of Δ_j subtended at \mathbf{x} . Finally

$$\begin{aligned}\vec{\Omega}_j(\mathbf{x}) &= \iint_{\Delta_j} \nabla' \frac{1}{|\mathbf{x}' - \mathbf{x}|} \times d\mathbf{S}' \\ &= \oint_{\Delta_j} \frac{1}{|\mathbf{x}' - \mathbf{x}|} d\mathbf{x}' \\ &= (\gamma_3 - \gamma_2)\mathbf{y}_1 + (\gamma_1 - \gamma_3)\mathbf{y}_2 + (\gamma_2 - \gamma_1)\mathbf{y}_3\end{aligned}\quad (21)$$

with

$$\begin{aligned}\gamma_k &= \frac{-1}{|\mathbf{y}_{k+1} - \mathbf{y}_k|} \\ &\quad \times \ln \frac{|\mathbf{y}_k||\mathbf{y}_{k+1} - \mathbf{y}_k| + \mathbf{y}_k \cdot (\mathbf{y}_{k+1} - \mathbf{y}_k)}{|\mathbf{y}_{k+1}||\mathbf{y}_{k+1} - \mathbf{y}_k| + \mathbf{y}_{k+1} \cdot (\mathbf{y}_{k+1} - \mathbf{y}_k)}.\end{aligned}\quad (22)$$

The integrals in (20) and (21) are derived in [11]. From (18) it follows that the method here described has the following interesting properties.

- 1) The perturbation field can be computed without matrix inversion.
- 2) For each point \mathbf{x} the same explicit expression can be used. The total computation time is therefore proportional to the number of points where the magnetic field needs to be computed.
- 3) The computation time is proportional to the number of triangles.
- 4) When the object contains a large flat part, that part of the surface may be described with one or a few large triangles, without influencing the accuracy. To proof this conclusion, consider a set of (small) adjacent triangles having the same normal \mathbf{n} . Their contribution to the sum in (18) consists of a constant factor, $\frac{\mathbf{x}^+ - \mathbf{x}^-}{4\pi} \mathbf{B}_0 \cdot \mathbf{n}$, multiplied with the integrals $\mathbf{n} \vec{\Omega}_j$ and $\mathbf{n} \times \vec{\Omega}_j$ which vary from triangle to triangle. The first of these integrals Ω_j is the solid angle of triangle j , subtended from \mathbf{x} . Since

the solid angle of a set of adjacent triangles equals the solid angle of the contour of the set, the integral over the set of triangles may be split into integrals over a few large triangles having the same contour. Similarly, the integrals $\vec{\Omega}_j$ can be expressed as contour integrals ([21]) and therefore the integral over the set of triangles only depends on the contour.

- 5) Triangles which are parallel to the homogenous magnetic field do not contribute to the surface integral.

D. A Method for Triangulation

When the method described above is applied in practice one has to derive a triangular grid for the surface of each compartment in the data set. First, the compartments have to be segmented and a uniform distribution of boundary points has to be determined. To segment the head or the brain from a single MR T1 image one can use, e.g., the method presented in [12]. Different solutions are described in the literature to derive a triangular grid for a given discrete set of points (e.g., [13], [14]). These methods in particular address the problem of reconstructing a 3-D data set from a set of 2-D intersections, thereby taking into account that an object may split into two or more contours on the same slice.

In the examples given in Section III the compartments have a sphere like topology. For these cases a triangulation can be determined readily by first projecting the boundary points on the unit sphere about the object's center of gravity. On this sphere a Delaunay triangulation is performed using the algorithm (and software) of [15]. We have found this method very stable for different objects like (truncated) spheres, cubes, and segmented heads from MR imaging.

To obtain a locally coarse grid on flat parts of the object, the flatness of the surface at a point \mathbf{x} was expressed using the solid angle Ω of the surface, subtended at \mathbf{x} . For smooth surfaces this solid angle equals 2π . For a polyhedron, like a triangulated surface, the solid angle can deviate substantially from 2π when \mathbf{x} is at a sharp corner (e.g., a vertex). At corners pointing to the outside of the object, the solid angle has a value near zero and at corners pointing to the inside the solid angle approaches 4π . Based on these properties, we use $|2\pi - \Omega_n|$ as a definition of the sharpness of point n on the surface. It varies from zero (smooth parts of the surface) to 2π for very sharp corners.

Using this definition of sharpness, the following algorithm was applied to obtain a coarse triangulation. First, a fine uniform grid is determined and a triangulation is performed using the sphere projection method. A coarse grid could be obtained by simply leaving out all points having a sharpness less than a threshold value Ω_{\max} . However, many "flat" points that are located close together may form a sharp corner that should not be deleted in the final geometrical description. Therefore, the following iterative method was used. All points having a sharpness less than Ω_{\max} or a nearest neighbor closer than d_{\min} but not having a neighbor with the same properties are tagged. All tagged points are left out and the remaining points are triangulated again. These steps are repeated until no more reduction of points occurs.

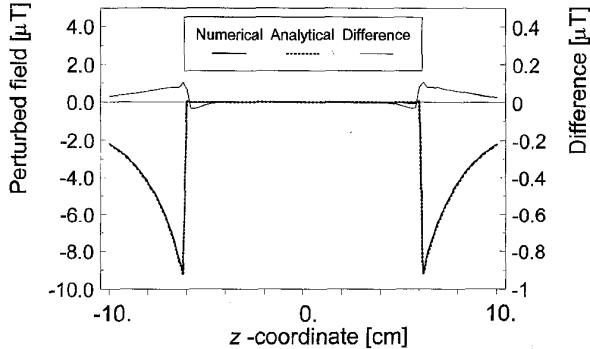


Fig. 2. The perturbation field of a sphere computed by the analytical formulas (dotted line) and computed by the numerical method described in the present paper (thick solid line). These two curves correspond to the left vertical scale. The thin solid line gives the difference between both methods as a function of z . This curve corresponds to the scale depicted at the right of the graph. The driving homogeneous field has a magnitude of 1.5 T and is pointing in the z -direction. The susceptibility of the sphere amounts to -10^{-5} and the susceptibility outside the sphere is assumed to be zero. The sphere has a radius of 6 cm. In the numerical computations this sphere was described with a grid consisting of 440 points and 876 triangles. The origin is at the center of the sphere.

The solid angle Ω_n of a vertex x_n can be computed as follows. If $\{x_{n1}, x_{n2}, x_{n3}, \dots, x_{nk}\}$ are the neighbors of x_n ordered in clockwise order, then

$$\Omega_n = \sum_{i=2}^k \Omega_{n_1 n_i n_{i+1}} \quad (23)$$

where here Ω_{ijk} is the solid angle of triangle Δ_{ijk} subtended from x_n . The latter solid angles can be computed using (20).

III. RESULTS

A. The Magnetic Field

To verify the validity of the described method, the boundary element solution [in the form of (18)] was compared with the analytical solution [16], [19] of a sphere with a constant susceptibility in a homogeneous magnetic field. The homogeneous field is directed in the z -direction and has a strength of 1.5 T. The susceptibility of the sphere, with radius of 6 cm, is assumed to be -10^{-5} , which is a realistic value for human tissue [1], [2]. Fig. 2 shows the z -component of the perturbation field computed along a line in the z -direction through the sphere. The dotted line is computed with the analytical formulas and the (thick) solid line is computed with the numeral method described here, using a grid consisting of 440 points and 876 triangles. The thin solid line represents the difference between both curves and is plotted using the scale at the right-hand side of the graph. The maximum difference occurs at the sphere boundary and is less than $0.109 \mu\text{T}$, which is about 0.072 ppm of the main magnetic field. Note that in both solutions the Lorentz correction [19] has been applied so that the perturbation field vanishes inside the sphere.

To compute the magnetic field perturbation caused by a realistic object, the procedure described in Section II-D was applied to a 3-D MR imaging data set of a human head. The fine triangular grid of the head is shown in Fig. 3(a). This

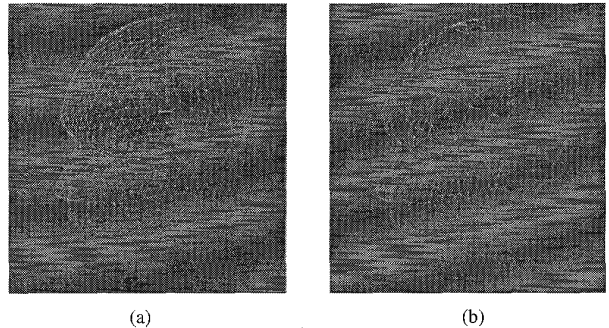


Fig. 3. Two triangulations of a 3-D MR imaging data set of the head are shown. (a) On the left a fine triangulation is shown consisting of 2000 points and 3996 triangles. (b) On the right the result of the point removal algorithm with $\Omega_{\max} = .5$ and $d_{\min} = 0.3$ cm. This object has approximately the same shape as the original object, but requires only about one third of the vertices.

grid consists of 2000 points and 3996 triangles. Redundant triangles were removed with $\Omega_{\max} = 0.5$ and $d_{\min} = 0.3$ cm (these numbers give satisfactory results in several realistic geometries). In this way, a grid was obtained with only 610 points and 1216 triangles but which has a similar geometrical shape, as shown in Fig. 3(b).

Fig. 4(a) shows the distribution of the z -component of the perturbation field in a vertical plane through the head. Positive values are represented in red, negative values are in blue, and zero is represented in black. The field was computed using the coarse triangulation of Fig. 3. Outside the head a dipolar pattern is present with a large negative jump at the top of the head. This jump is similar to the one shown in Fig. 2 for the sphere. Inside the head the field is close to zero (the Lorentz correction was applied) except for a positive field present at the bottom end of the scan. Furthermore, there are some small scale variations about the nose and eye region.

The positivity inside the head is an artifact caused by the absence of scan data outside the field of view (FOV). To verify this hypothesis we plotted in Fig. 5(b) the computed magnetic induction field along the symmetry axis of a truncated sphere. About 1 cm was cut from the bottom end of a sphere with radius of 6 cm [Fig. 5(a)]. A positive peak arises at the sphere boundary, which is absent in the complete field of the sphere (dotted line). This effect was also observed in other geometries (cylinders and blocks) with a relatively large flat part perpendicular to the applied homogeneous field. The field outside the opposite part of the truncation is hardly effected by the cut [Fig. 5(b)].

The “missing data effect” is caused by the contribution of an artificial interface to the boundary integral in (17). A simple solution for the missing data problem is to leave out this interface from the surface integral. Because it was observed that surface elements parallel to the main magnetic field do not contribute to the perturbation field (18), the geometrical meaning of this solution is that at the data boundary the object extends to infinity in the form of a generalized cylinder. For most anatomical sites, e.g., head, neck, and pelvis, this assumption is much more realistic than the assumption that the object vanishes outside the FOV.

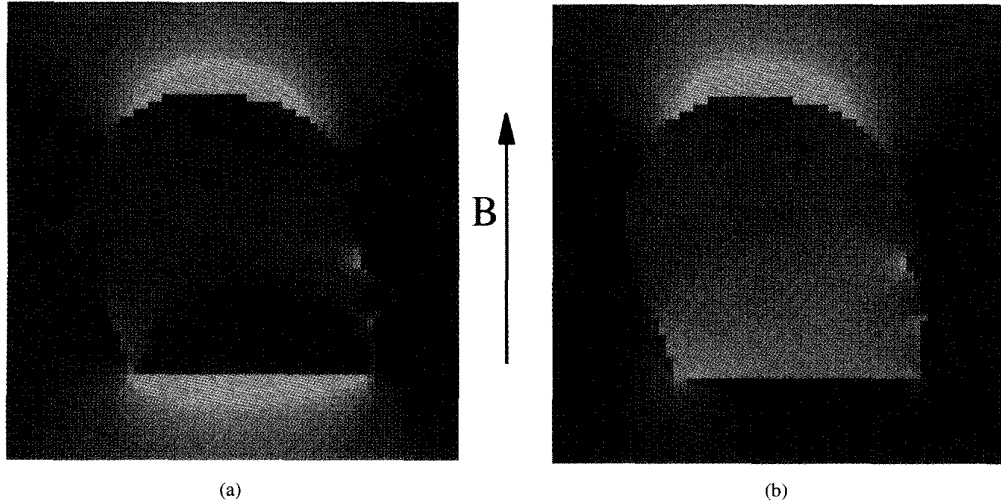


Fig. 4. The distribution of the vertical component of the perturbation field in a realistic object. This object represents a head derived from a 3-D MR imaging data set. Positive values (parallel to B_0) are represented in red, negative values (anti parallel to B_0) are represented in blue and zero values are represented in black). (a) An artifact induced by the missing data at the neck region. In (b) it was attempted to reduce this artifact by disregarding the artificial horizontal plane at the bottom end of the object.

Fig. 4(b) presents the perturbation field computed similar to the one presented in Fig. 4(a), after leaving out the bottom triangles of Fig. 3(b). The field outside the head appears to be hardly effected and also the small scale variations at the eyes, mouth and nose are similar. The large scale variations in the head are, as expected, significantly different. Along a vertical line through the middle of the head it varies almost linearly over a range of about $5 \mu\text{T}$ from top to bottom. The large positive field at the interface has disappeared.

B. Distortions

The magnetic field computations can be used to simulate and quantify MR image distortions. For a 2-D Fourier MR measurement set up with spin echo, a slice selection gradient of G_z and a readout gradient of G_y , the pixel displacement in the z and y direction is given by [16], [17]

$$\delta z = -\delta B_0/G_z \quad \text{and} \quad \delta y = \delta B_0/G_y. \quad (24)$$

The distortions in the x -direction (phase encoding) vanishes. In the following computations we took $B_0 = 1.5 \text{ T}$, $G_y = G_z = 1.5 \text{ mT/m}$, and $\chi = -10^{-5}$. Furthermore, the object was reduced 1% with respect to its center of gravity so that the field points on which the distortions were computed were just outside the object's boundary. The average distance between the original and "shrunk" point set was .11 cm. This was necessary because at the surface the magnetic induction is mathematically not defined. Finally, the fine grid of Fig. 3(a) was used in the computations. Note that the gradient fields in modern commercial scanners are a factor of two higher, resulting in a reduction of the distortion by a factor of two. The numbers given here represent a worst case.

Fig. 6 shows the distortions viewed from two different directions. The original object is represented by flat triangles and the distorted object by a net of open triangles. The upper part is displaced vertically outward the object and the left and right side are moved to the right. However, this distortion

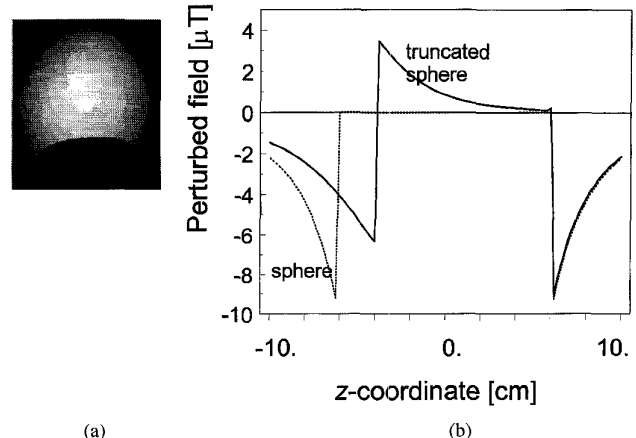


Fig. 5. (a) The missing data effect simulated by a truncated sphere. (b) The graph was computed with the same conditions as applied in Fig. 2. A layer about 1 cm was cut off from the bottom of the sphere, resulting in an object consisting of 374 points and 744 triangles.

can not be considered as a simple translation, because some points are moving inward. To quantify the magnitude of the distortions, we plotted in Fig. 7 the histogram of δy . There are two peaks at about plus and minus 0.5 cm. The histogram for δz has a similar shape, as follows from (24). Therefore, the average displacement of the points just outside the head amounts to about $0.5 \cdot \sqrt{2} \approx 0.7 \text{ cm}$.

IV. DISCUSSION AND CONCLUSION

This paper shows that the BEM, with its approximation for small χ , is well suited for efficiently computing the magnetic field at a limited number of points, e.g., a 2-D surface or a set of markers. The computer time required to compute the distorted object (Fig. 6) is of the same order as the time required for the segmentation (which has to be done with any method) and triangulation. With conventional methods the

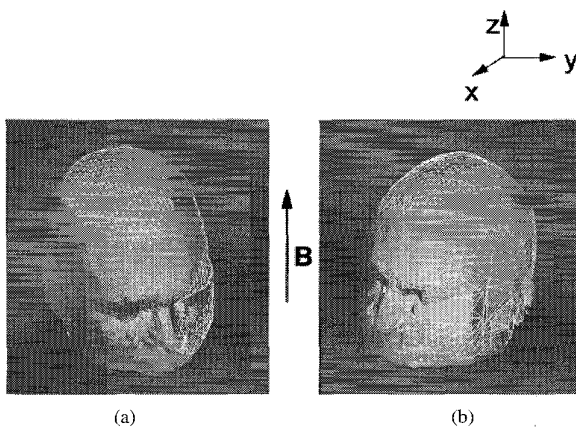


Fig. 6. The undistorted object and its distortion just outside the surface are plotted together, viewed from two different directions. The distortions were computed using a slice selection and a read out gradient of 1.5 mT/m and a homogeneous field of 1.5 T . The distortion in the x -direction (front to back) is zero. To compute these images a fine grid with 2000 points was used.

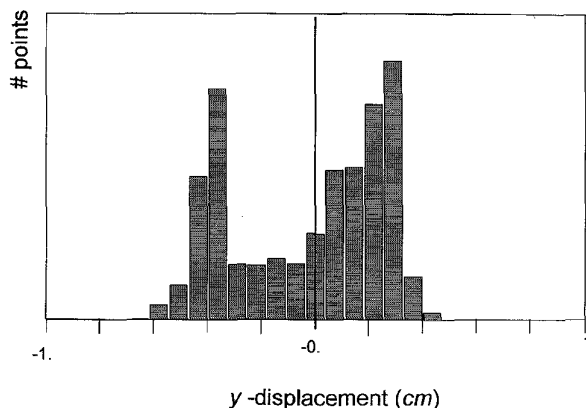


Fig. 7. The displacement histogram of corresponding displacements of the y -coordinates over the surface shown in Fig. 6. The total number of points equals 2000.

magnetic field must first be computed for the complete volume and the surface or the marker positions must be selected afterwards. For a complete 3-D field (Fig. 4) the computation time is similar to the time needed by the 3-D finite difference method of [5].

In this study equation (18) was implemented in a straightforward way. However, the method can be optimized by precomputing the line integrals over the edges (22). This approach will save about 40% of time, assuming that the computational costs of (20) and (22) are equal. Furthermore, fast approximations of (20) and (22) can be used when the distance between the view point and the triangle is large compared to the size of the triangle. In these conditions, the solid angle (20) approaches a dipole potential and the line integral in (21) tends to a monopole potential.

The BEM gives a practical way of dealing with the missing data problem. By simply leaving out some triangles, the part of the object outside the FOV is modeled as a generalized cylinder that extends to infinity. In the case of the human head presented here, the part of the object immediately outside

the FOV is the neck region and therefore a cylinder is quite appropriate. More important, our results show that this way of modeling has a major effect on the computed magnetic field inside the head (Fig. 4) and cannot be ignored. For alternate methods to compute the magnetic field no such simple way of modeling the object exists.

The BEM is based on the assumption that the object consists of compartments which have a constant susceptibility. With alternate methods the magnetic field can be computed for objects having a susceptibility which varies from point to point. However, for the application with MR this is only a theoretical advantage because the true susceptibility distribution is not known in practice and approximate values are used for each type of tissue. Such data is presented e.g., in [2]. The largest susceptibility difference in human tissue [except lung ($\chi = -5 \cdot 10^{-6}$)] is between fat ($\chi = -7 \cdot 10^{-6}$) and oxygenated blood ($-9.31 \cdot 10^{-6}$). Since these differences are small, a head with a constant susceptibility is a realistic assumption.

This study explores the behavior of MR image distortions, with the ultimate goal to improve the registration of MR and CT images [28] by including realistic nonlinear deformations. Alternative methods for correcting distortions caused by static field inhomogeneity are described in [3] and [17]. Those methods require the acquisition of an additional MR image with a reversed gradient [17] or a different echo time [3], thereby increasing the data acquisition time by a factor of two. The advantage of those methods is that they automatically include the susceptibility effects of e.g., a stereotactic frame or the presence of magnetizable material on the patient. With our method these effects have to be modeled separately.

Our simulations show that distortions caused by susceptibility differences occur both on a large scale and on a small scale (at the nose, eyes and ears). Outside the head the large scale perturbation field has a dipolar structure. This information can be used to predict the distortion of markers that are fixed upon the skin of the patient [29]. Inside the head the perturbation field varies almost linearly from top to bottom. In the case presented in Fig. 4(b) a homogeneous field of 1.5 T was assumed and a susceptibility of -10^{-5} , resulting in a perturbation field which varies over a range of $5 \mu\text{T}$ from top to bottom. Therefore, the susceptibility effect causes an additional vertical gradient of about $.025 \text{ mT/m}$. When for the slice selection a vertical gradient of 2.5 mT/m is used one expects to find a stretching of the MR image of about 1% in the vertical direction. This effect is roughly consistent with the amount of stretching we regularly find when matching MR images to CT images. In a follow up study these theoretical predictions will be tested experimentally in a more systematic way for several anatomical sites.

ACKNOWLEDGMENT

The authors wish to thank H. Bartelink, R. de Boer, and B. Mijnheer for their helpful comments.

REFERENCES

- [1] T. S. Sumanaweera, G. H. Glover, S. Song, J. R. Adler, and S. Napel, "Quantifying MRI geometric distortions in tissue," *Magn. Res. Med.*, vol. 31, pp. 40–47, 1994.

- [2] R. Bhagwandien, "Object induced geometry and intensity distortions in magnetic resonance imaging," Ph.D. dissertation, Univ. of Utrecht, Utrecht, 1994.
- [3] T. S. Sumanaweera, G. H. Glover, T. O. Binford, and J. R. Adler, "MR Susceptibility misregistration correction," *IEEE Trans. Med. Imag.*, vol. 12, no. 2, pp. 251–259, 1993.
- [4] R. Bhagwandien, R. v. Ee, R. Beersma, C. J. G. Bakker, M. A. Moerland, and J. J. W. Lagendijk, "Numerical analysis of the magnetic field for arbitrary susceptibility distributions in 2-D," *Magn. Res. Med.*, vol. 10, pp. 299–313, 1992.
- [5] R. Bhagwandien, M. A. Moerland, C. J. G. Bakker, R. Beersma, and J. J. W. Lagendijk, "Numerical analysis of the magnetic field for arbitrary susceptibility distributions in 3-D," *Magn. Res. Med.*, vol. 12, pp. 101–107, 1994.
- [6] J. T. Oden and J. N. Reddy, *An Introduction to the Mathematical Theory of Finite Elements*. New York, Wiley, 1976.
- [7] G. W. Pruis, B. H. Gilding, and M. J. Peters, "A comparison of different numerical methods for solving the forward problem in EEG and MEG," *Physiol. Meas.*, vol. 14, pp. A1–A9, 1993.
- [8] A. C. L. Barnard, I. M. Duck, and M. S. Lynn, "The application of electromagnetic theory to electrocardiology. I. Derivation of the integral equations," *Biophys. J.*, vol. 7, pp. 443–462, 1967.
- [9] D. B. Geselowitz, "On bioelectric potentials in an inhomogeneous volume conductor," *Biophys. J.*, vol. 7, pp. 1–17, 1967.
- [10] M. S. Hämäläinen and J. Sarvas, "Realistic conductivity geometry model of the human head for the interpretation of neuromagnetic data," *IEEE Trans. Biomed. Eng.*, vol. 36, no. 2, pp. 165–171, 1989.
- [11] J. C. de Munck, "A linear discretization of the volume conductor boundary integral equations using analytically integrated elements," *IEEE Trans. Biomed. Eng.*, vol. 39, no. 9, pp. 986–989, 1992.
- [12] M. E. Brummer, R. M. Mersereau, R. L. Eisner, and R. R. J. Lewine, "Automatic detection of brain contours in MRI data sets," *IEEE Trans. Med. Imag.*, vol. 12, no. 2, 1993.
- [13] J. D. Boissonat, "Shape reconstruction from planar cross sections," *Comput. Vision, Graph. Image Processing*, vol. 44, no. 1, pp. 1–29, 1988.
- [14] D. Meyers and S. Skinner, "Surfaces from contours," *ACM Trans. Graphics*, vol. 11, no. 3, pp. 228–258, 1992.
- [15] R. J. Renka, "Interpolation of data on the surface of a sphere," *ACM Trans. Math. Software*, vol. 10, no. 4, pp. 417–436, 1984.
- [16] K. M. Lüdeke, P. Röchmann, and R. Tischer, "Susceptibility artifacts in NMR Imaging," *Magn. Res. Med.*, vol. 3, pp. 329–343, 1985.
- [17] H. Chang and J. M. Fitzpatrick, "A technique for accurate magnetic resonance imaging in the presence of field inhomogeneities," *IEEE Trans. Med. Imag.*, vol. 11, no. 3, pp. 319–329, 1992.
- [18] D. D. Stark and W. G. Bradley, *Magnetic Resonance Imaging*. Chicago, 1992.
- [19] S. C. K. Chu, Y. Xu, J. A. Balschi, and C. S. Springer, Jr., "Bulk magnetic susceptibility shifts in NMR studies of compartmentalized samples: Use of paramagnetic reagents," *Mag. Res. Med.*, vol. 13, pp. 239–262, 1990.
- [20] M. R. Willcott III, G. L. Mee, and J. P. Chesick, "Magnetic field mapping in NMR Imaging," *Mag. Res. Imag.*, vol. 5, pp. 301–306, 1987.
- [21] C. J. G. Bakker, R. Bhagwandien, and M. A. Moerland, "Simulation of susceptibility artifacts in 2-D and 3-D Fourier Transform spin echo and gradient echo magnetic resonance imaging," *Mag. Res. Imag.*, vol. 12, pp. 767–774, 1994.
- [22] M. H. Phillips, M. Kessler, F. Y. S Chang, K. A. Frankel, J. T. Lyman, J. I. Fabrikant, and R. P. Levy, "Image correlation of MRI and CT in treatment planning for radiosurgery of intracranial vascular malformations," *Int. J. Rad. Oncol. Biol. Phys.*, vol. 20, pp. 881–889, 1991.
- [23] C. J. Henri, D. L. Collins, and T. M. Peters, "Multimodality image integration for stereotactic surgery planning," *Med. Phys.*, vol. 18, pp. 167–177, 1991.
- [24] M. Goitein, "Calculation of the uncertainty in the dose delivery during radiation therapy," *Med. Phys.*, vol. 12, pp. 608–612, 1985.
- [25] M. A. Moerland, R. Beersma, R. Bhagwandien, H. K. Wijrdeman, and C. J. G. Bakker, "Analysis and correction of geometric distortions in 1.5 T magnetic resonance images for use in radiotherapy treatment planning," *Phys. Med. Biol.*, submitted, 1995.
- [26] R. K. TenHaken, A. F. Thorton, H. M. Sandler, M. L. Lavigne, D. J. Quint, B. A. Fraass, M. L. Kessler, and D. L. McShan, "A quantitative assessment of the addition of MR to CT based 3-D treatment planning of brain tumors," *Radiother. Oncol.*, vol. 25, pp. 121–133, 1992.
- [27] J. D. Jackson, *Classical Electrodynamics*. New York, Wiley, 1975.
- [28] M. B. van Herk and H. M. Kooy, "Automatic three-dimensional correlation of CT-CT, CT-MR and CT-SPECT using chamfer matching," *Med. Phys.*, vol. 21, no. 7, pp. 1163–1178, 1994.
- [29] M. A. Moerland, R. Beersma, R. Bahgwandien, H. K. Wijrdeman, and C. J. G. Bakker, "Analysis and correction of geometric distortions in 1.5 T magnetic resonance images for use in radiotherapy treatment planning," *Phys. Med. Biol.*, vol. 40, pp. 1651–1664, 1995.